Journal of Rock Mechanics and Geotechnical Engineering 14 (2022) 108–122

Contents lists available at ScienceDirect

Journal of Rock Mechanics and Geotechnical Engineering

journal homepage: www.jrmge.cn

Full Length Article

Convective heat transfer of water flow in intersected rock fractures for enhanced geothermal extraction

Yuedu Chen, Zhihong Zhao*, Huan Peng

Department of Civil Engineering, Tsinghua University, Beijing, 100084, China

ARTICLE INFO

Article history:
Received 11 January 2021
Received in revised form
15 April 2021
Accepted 9 May 2021
Available online 10 July 2021

Keywords:
Heat transfer
Fracture intersection
Fluid flow
Rough fracture
Geothermal extraction

ABSTRACT

Numerous intersected rock fractures constitute the fracture network in enhanced geothermal systems. The complicated convective heat transfer behavior in intersected fractures is critical to the heat recovery in fractured geothermal reservoirs. A series of three-dimensional intersected fracture models is constructed to perform the flow-through heat transfer simulations. The geometry effects of dead-end fractures (DEFs) on the heat transfer are evaluated in terms of intersected angles, apertures, lengths, and the connectivity. The results indicate that annular streamlines appear in the rough DEF and cause an ellipse distribution of the cold front. Compared to plate DEFs, the fluid flow in the rough DEF enhances the heat transfer. Both the increment of outlet water temperature ΔT_{out} and the ratio of heat production Q_r present the largest at the intersected angle of 90° while decline with the decrease of the intersected angle between the main flow fracture (MFF) and the DEFs. The extension of the length of intersected DEFs is beneficial to heat production while enhancing its aperture is not needed. Solely increasing the number of intersected DEFs induces a little increase of heat extraction, and more significant heat production can be obtained through connecting these DEFs with the MFF forming the flow network.

1. Introduction

Geothermal resources are treated as a fully renewable and sustainable energy, which provides a robust, long-lasting option that complements other important contributions from clear coal, nuclear, solar, wind, hydropower, and biomass (Tester et al., 2006; Cao et al., 2016; Liu et al., 2019, 2020; Zinsalo et al., 2020). The sufficient thermal extraction from subsurface geothermal reservoirs relies upon creating or accessing an open and connected fracture system, through which the injection water flowing within the reservoir can be heated by contact with hot rocks and then brings the heat to the surface by the fluid circulation (Fig. 1a). Understanding the heat transfer behavior within the subsurface fracture network is therefore crucial for the geothermal reservoir management in terms of optimizing the heat extraction and improving the heat-recovery factor of geothermal reservoirs (Xu et al., 2015; Lepillier et al., 2020).

Geothermal systems are usually established in the fractured formation, which is observed through the acoustic image logs to indicate that intersected natural fractures or geologically weak planes, including partly sealed fractures, microfractures, and major fractures, provide possible fluid pathways (Vidal et al., 2017). However, the natural fracture network consists mainly of dead-end fractures (DEFs) (Fig. 1d), which are not well connected to form the commercial-size reservoir (Tester et al., 2006). Thus, the fractured formation must be hydraulically stimulated to create new artificial fractures, which are allowed to connect pre-existing fractures to increase the permeability and heat transport (Fig. 1b). Hydraulic fractures encountering a natural fracture can either arrests, cross, or be deviated by the natural fracture (Lepillier et al., 2020; Sanchez et al., 2020). When the hydraulic pressure exceeds the rock tensile strength but is less than the shear strength of the natural fracture (Zhou et al., 2020), the hydraulic fracture can propagate across the weak plane. Therefore, the intersection of hydraulically stimulated and natural (dead-end) fractures affects heat exchange between the working fluid and the hot rock, which is an important concern for the heat extraction (Turan et al., 2016; Zhang et al., 2019a).

Numerous simulation studies have focused on the heat transport in intersected fractures or discrete fracture networks (Shaik et al., 2011; Gan and Elsworth, 2016; Sun et al., 2017; Chen et al., 2018, 2019a, 2020a; Song et al., 2018; Zhang et al., 2019b; Gong et al., 2020). The common method is regarding the crack as a planar object splitting

* Corresponding author.
E-mail address: zhzhao@tsinghua.edu.cn (Z. Zhao).

Peer review under responsibility of Institute of Rock and Soil Mechanics, Chinese Academy of Sciences.

https://doi.org/10.1016/j.jrmge.2021.05.005

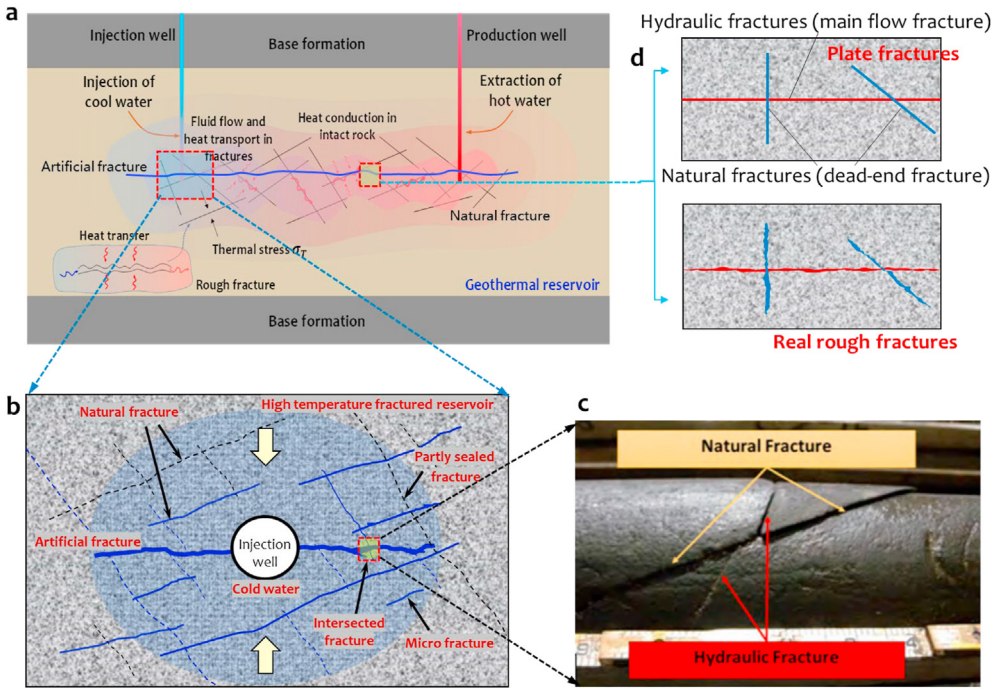

Fig. 1. (a) Schematic view of the heat transfer in a fractured geothermal reservoir; (b) Schematic diagram of the hydraulically induced artificial tensile fractures and pre-existing natural fractures in a high-temperature fractured reservoir; (c) An example of a hydraulic fracture cutting a natural rough fracture captured in the core (Vidal et al., 2017); and (d) Conceptual illustrations of the intersection of hydraulically stimulated fractures propagating across dead-end natural fractures in the enhanced geothermal extraction in terms of plate fractures and real rough fractures (Sanchez et al., 2020).

the material into two parts with a displacement discontinuity (Selvadurai et al., 2015; Lepillier et al., 2020) (Fig. 1d). The change in fracture aperture caused by thermoelastic and poroelastic deformations significantly affects fluid flow and heat transfer in fractures (Salimzadeh et al., 2018; Vik et al., 2018; Kadeethum et al., 2019). Salimzadeh et al. (2018) found that the matrix contraction due to the cooling of the matrix increases the fracture aperture and facilitates the creation of favorable flow pathways. Guo et al. (2016) investigated that the non-uniform temperature decrease in the rock body makes the flow increasingly concentrated into some preferential paths through the action of thermal stress. Besides, the fracture network distribution also affects the heat transfer. Ma et al. (2020) indicated that the shape of the cold front is closely related to the position of two intersected fractures, and the more uniform distribution of fractures in reservoirs will accelerate the heat extraction of the flowing water from surrounding reservoirs. Zhang et al. (2019c) concluded that the increase of the fracture density in the random distribution fracture network enhances the flow around and retards thermal drawdown. However, Shi et al. (2019a) obtained an opposite result that vast fractures provide too many preferential flow channels for the working fluid and accelerate the thermal breakthrough, and the discrete fracture network with fewer and longer fractures is beneficial to the heat extraction under the same fracture density. Qu et al. (2017) indicated that the increasing complexity of the fracture network is favorable for heat mining, and the lengths and numbers of branch fractures affect the heat mining. Shi et al. (2019b) indicated that the natural and non-planar fractures are critical to accurately estimate the enhanced geothermal system performance, and the shorter primary and longer secondary fractures improve the production temperature. Fu et al. (2016) highlighted that intensively inter-connected fractures offer low hydraulic impedance but do not improve the heat production performance. Although the above researches deeply analyzed the effects of geometry characteristics of fracture networks on the heat transfer process and provided instructions for the optimum selection of the reservoir stimulation scheme (Ma et al., 2020), most studies regarded the fracture as a plate (Fig. 2b) (Zhao et al., 2015; Ma et al., 2020) or a hypothetical rough fracture (Aliyu and Chen, 2017a; Yao et al., 2018), which contains uniform aperture distribution between two rough surfaces (Chen and Zhao, 2020). Neglecting the heterogeneous apertures in the real rock fracture (Fig. 2c) would omit the channeling flow and misestimate the temperature evolution and heat transport (Chen and Zhao, 2020). The complex heat transfer within multiple fracture channels is also not well evaluated.

Both stimulated and natural fractures are intrinsically heterogeneous (Pyrak-Nolte and Nolte, 2016; Chen et al., 2019b). The fracture geometries, including roughness, void space and contact area, complicate the heat transfer within rock fractures (Huang et al., 2016). By comparing the heat transfer through the smooth and rough fractures, the roughness geometries are found to affect the heat flux distribution at the fracture–rock interface for low and high Péclet numbers (Andrade et al., 2004; Ma et al., 2018). The increase of the surface roughness can enhance the heat transfer compared with the smooth fracture (Ma et al., 2018; He et al., 2019). Besides, the hydraulic apertures (Nigon, 2018; Bakker et al., 2019) are also found to be critical to the heat transfer process. The local heat transfer coefficient is closely dependent on the fluctuation of the fracture morphology and apertures (He et al., 2016). These findings confirm the importance of heterogeneous fracture geometries on heat transfer in single rock fractures. Thus, it can be further launched that the irregular intersection zones formed by two three-dimensional (3D) rough fractures, showing great differences from the plate intersection (Fig. 2b), will complicate the heat transfer process. Therefore, evaluating the heat transfer behavior of the cool water flow through the 3D intersected rough fracture with heterogeneous apertures is urgently needed for the geothermal extraction modeling, especially when the dead-end natural fractures are considered (Fig. 1d), which are more realistic than the smooth parallel plates in previous simulations.

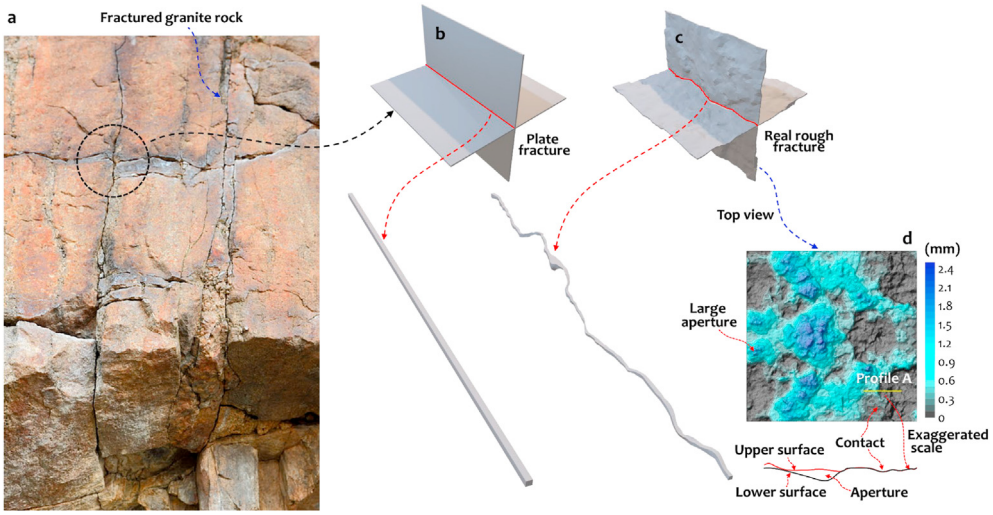

Fig. 2. (a) Schematic diagram of the naturally fractured granite (Huang et al., 2016); (b, c) Illustration of plate and real rough three-dimensional (3D) intersected rock fractures, respectively; and (d) Heterogeneous distribution of apertures in the 3D real rough rock fracture, and the color bar indicates the aperture range.

The main aim of this study is to advance our understanding of the heat transfer in 3D intersected rough fractures in terms of (1) understanding the heat transfer behavior in variable 3D intersected geometric configurations of DEFs and main flow fractures (MFFs), and (2) providing some insights of determining the main factors that affect the heat transfer. Based on this purpose, a series of 3D intersected fracture models with various intersection geometries was built to perform the flow-through heat transfer simulations by solving hydrothermal coupling equations, to examine how the geometries of intersected DEFs, including heterogeneous apertures, intersected angles, apertures, lengths, and the connectivity, affect the heat transfer behavior in 3D intersected geometries for the fractured geothermal extraction. All modeling cases were conducted under three different injection velocities.

2. Modeling description

Hydrothermal coupling processes during the geothermal exploitation can be simplified with several assumptions:

(1) The granite matrix is assumed as impermeable compared to the fracture that provides the main channel of the heat and energy recovery.
(2) The local thermal equilibrium (LTE) assumption is adopted to describe the continuity of the temperature from the fracture surface to the fluid at local points.
(3) The inertial force arisen from high flow velocity is neglected compared to the viscous force.

2.1. Governing equations

The computational modeling of the flow in a rough fracture is achieved by solving Navier-Stokes equations (NSEs) (Xiong et al., 2018), which are governed by the mass and momentum conservation equations. For an incompressible and isothermal single Newtonian fluid flow, the NSEs can be written as (Bear, 1972; Zou et al., 2017):

$$\nabla\cdot\boldsymbol{u} = 0 \tag{1}$$

$$\rho_f\frac{\partial\boldsymbol{u}}{\partial t} + \rho_f(\boldsymbol{u}\cdot\nabla)\boldsymbol{u} = -\nabla P + \mu\nabla^2\boldsymbol{u} \tag{2}$$

where $\boldsymbol{u}$ is the flow velocity vector, P is the fluid pressure, ρ_f is the fluid density, and μ is the dynamic viscosity. In Eq. (2), the convective acceleration term $(\boldsymbol{u}\cdot\nabla)\boldsymbol{u}$, representing the inertial force acting on the fluid, gives rise to the nonlinearity of the equation and makes the exact solution of Eq. (4) difficult to be obtained, especially for a rough rock fracture (Xiong et al., 2011). In certain cases, where the inertial force in the fluid is negligibly small compared with the viscous force and pressure (Koyama et al., 2009), the NSEs can be reduced to the Stokes' equation $\rho_f(\partial\boldsymbol{u}/\partial t) = -\nabla P + \mu\nabla^2\boldsymbol{u}$, which is suitable for simulating the low Reynolds number (Re) flow through rough rock fractures and conduits (Selvadurai et al., 2017). This study focuses on the flow and heat transport at low flow velocities and Stokes' equation is therefore considered.

The heat transfer in the fracture fluid is predominantly governed by the convection and conduction, and the energy conservation equation of the fluid in fractures is expressed as (Wang et al., 2019):

$$\rho_f C_{p,f}\frac{\partial T}{\partial t} + \rho_f C_{p,f}\boldsymbol{u}\cdot\nabla T_f + \nabla\cdot\left(-K_f\nabla T_f\right) = -\boldsymbol{n}\cdot K_f\nabla T_f \tag{3}$$

where $C_{p,f}$ is the specific heat capacity of the fluid at constant pressures; T_f and K_f are the temperature and heat conduction coefficient of the fluid, respectively; t is the time; and $\boldsymbol{n}$ is the normal vector of the fracture surface.

The heat transfer in the rock is mainly governed by the conduction, and the governing equation for the conservation of energy in the rock is expressed as

$$\frac{\partial}{\partial t}(\rho_s C_s T)_s = \nabla\cdot(K_s\nabla T_s) \tag{4}$$

where ρ_s is the solid density; C_s is the solid specific heat capacity; and T_s and K_s are the absolute temperature (K) and heat conduction coefficient of the rock, respectively.

The coupling between the fluid flow and heat transfer is carried out through the temperature-dependent parameters, including ρ_f, $C_{p,f}$, μ and K_f. The coupling between the heat transport and fluid flow is achieved through the velocity term (the contribution of convective heat transport) in Eqs. (3) and (4) (Aliyu and Chen, 2017b).

2.2. Model verification

Owing to the lack of experimental results to validate above mathematical models, the theoretical results through solving the flow and heat transfer in a conceptual two-dimensional (2D) single fracture model are used for verification (Fig. 3). The single fracture model with the length L and height $2R$ is maintained with a constant wall temperature T_0. The water with the temperature T_{in} and velocity v is injected into the fracture and flows out from the right with the temperature T_{out}. If the thermal diffusion in the fluid is not considered, the analytical solution of the water temperature T_f is calculated (Zhao, 2014):

$$T_f(x) = T_0 + (T_{in} - T_0)\exp\left(-x\frac{K_r}{v\rho_w C_w bR}\right) \quad (5)$$

where ρ_w and C_w are the density and specific heat capacity of the water, respectively; K_r is the rock heat conductivity coefficient; and b is the half aperture of the fracture.

Here, the steady flow and heat transfer in a rectangular region ($L = 1$ m, $R = 0.25$ m, $b = 10$ μm) are modeled by using the above mathematical models. The parameters used in numerical and analytical solutions are listed in Table 1. Fig. 4 compares the numerical and analytical results of the water temperature. The maximum error between them is only 1.4%, indicating that the proposed mathematical models are reliable to describe the flow and heat transfer in rock fractures.

3. Computational models of 3D intersected rock fractures

3.1. Computational geometries

A cubic computational model with a side length of 2 m is built (Fig. 5). Two 3D intersected fractures, including a horizontal MFF and an intersected DEF, are embedded in the model. The surface geometries of these two fractures are upscaled from the scanning data of the laboratory-scale Brazilian-induced tensile and natural granite fractures (Chen et al., 2020b), respectively. The initial temperature (423.15 K) over the whole computational domain is constant based on the actual temperature of the geothermal reservoirs at depths of approximately 4000 m. The temperatures at the top, bottom, and back faces of the computational domain are also 423.15 K. All fracture surfaces and lateral boundaries are specified as impervious, i.e. $\partial h/\partial \boldsymbol{n} = (\nabla h)\cdot\boldsymbol{n}$, and non-slip boundaries, i.e. $\boldsymbol{u} = 0$. The water with a low temperature of 313.15 K and a constant velocity is injected at the left end. The rock walls at the inlet and outlet, as well as the front boundary of the model, are treated as adiabatic.

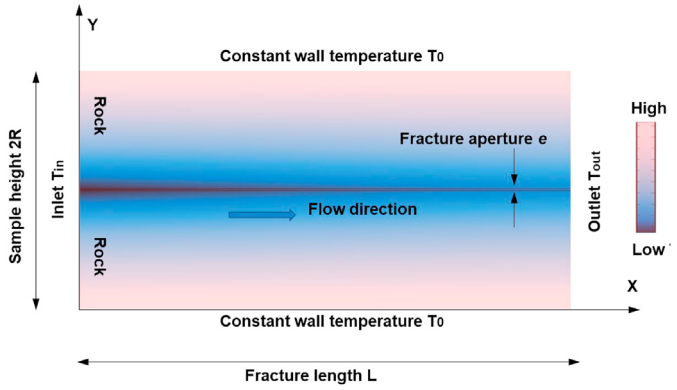

Fig. 3. Schematic diagram of the heat transfer in a 2D single fracture model (Wang et al., 2019).

Table 1
Model parameters for numerical and analytical solutions.

Parameter	Unit	Value
Wall temperature	°C	120
Injection water temperature	°C	30
Density of water	kg/m^3	1000
Specific heat capacity of water	J/(kg K)	4200
Specific heat capacity of granite	J/(kg K)	1000
Heat conductivity of granite	W/(m K)	2.4
Injection flow velocity	m/s	0.002

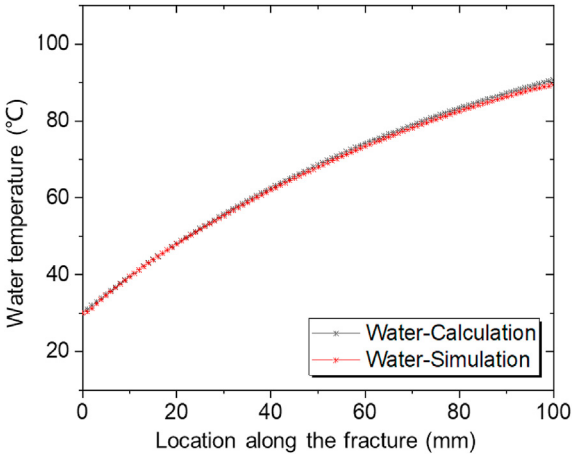

Fig. 4. Comparison of numerical and analytical results of the water temperature.

3.2. Model meshing

An example of the meshing of the fractured model is illustrated in Fig. 6, in which the meshes around two intersected rock fractures are refined to improve the simulation. Preliminary investigations show that, when the grid number exceeds 14 million, the average outlet temperature changes little, but the computational time increases significantly. Considering the computational time and accuracy, an average of about 14 million tetrahedral grids are set up for the simulation. The study aims to reveal the heat transfer mechanism in intersected fractures and the simulation time is not necessary as long as months or years. Thus, a heat transfer period of 240 h with a time step of 0.3 h is solved using the transient solver. The hydraulic and thermal properties of the water vary with temperatures (Freels et al., 2010). For the granite, the density is 2643 kg/m^3, the specific heat capacity is 1000 J/(kg K), and the heat conductivity is 2.4 W/(m K).

3.3. Simulation procedures

The intersected geometries, including intersected angles, apertures, lengths, and the connectivity, would be changed due to the hydraulic fracturing during the geothermal extraction. To investigate the influence of these factors on heat transfer through intersected fractures, three modeling scenarios are proposed:

(1) Modeling scenario I investigates the effect of intersected angles, including 20°, 55°, 90°, 125°, and 155°, on the heat transfer behavior in rock fractures. Meanwhile, to highlight the influence of heterogeneous apertures, a group of 3D intersected plate fractures (Fig. 7a) were modeled similarly for comparison. The mechanical apertures of the horizontal MFF and the intersected DEF in plate models are equal to

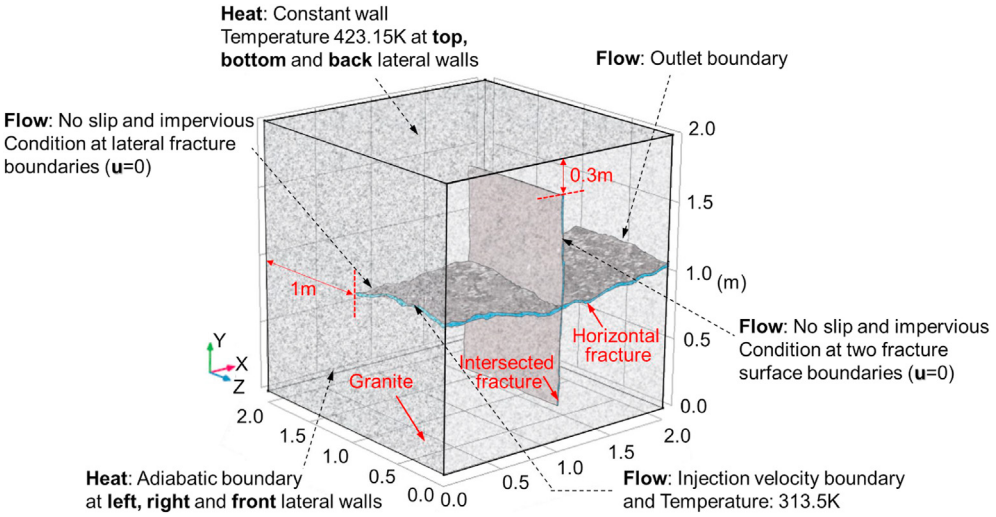

Fig. 5. A 3D intersected fracture model and the boundary conditions.

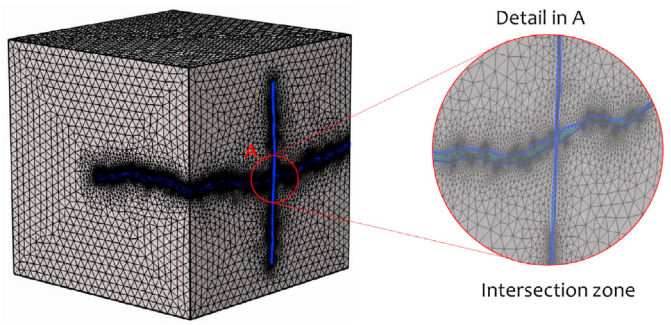

Fig. 6. An example of the meshing of 3D intersected fracture models.

those of rough models. Three injection velocities, 0.0002 m/s, 0.002 m/s and 0.2 m/s, are considered.

(2) Modeling scenario II investigates the effects of apertures and lengths of the intersected DEF on the heat transfer behavior (Fig. 8). Here the aperture refers to the mechanical aperture, which increases from 0.082 mm to 0.432 mm. The length increases from 2 mm to 15 mm. The boundary conditions are the same as before (Fig. 5). Three injection velocities, 0.0002 m/s, 0.002 m/s and 0.02 m/s, are considered.

(3) Modeling scenario III investigates the effect of the connectivity of the intersected DEF on the heat transfer behavior (Fig. 9). Model M1 with three unconnected intersected DEF and model M2 with seven connected intersected DEF (Fig. 9) are built to compare with the intersected single fracture model M0. The boundary conditions are the same as before (Fig. 5). Three injection velocities, 0.0002 m/s, 0.002 m/s and 0.02 m/s, are considered. All geometric information of three modeling scenarios is included in Table 2.

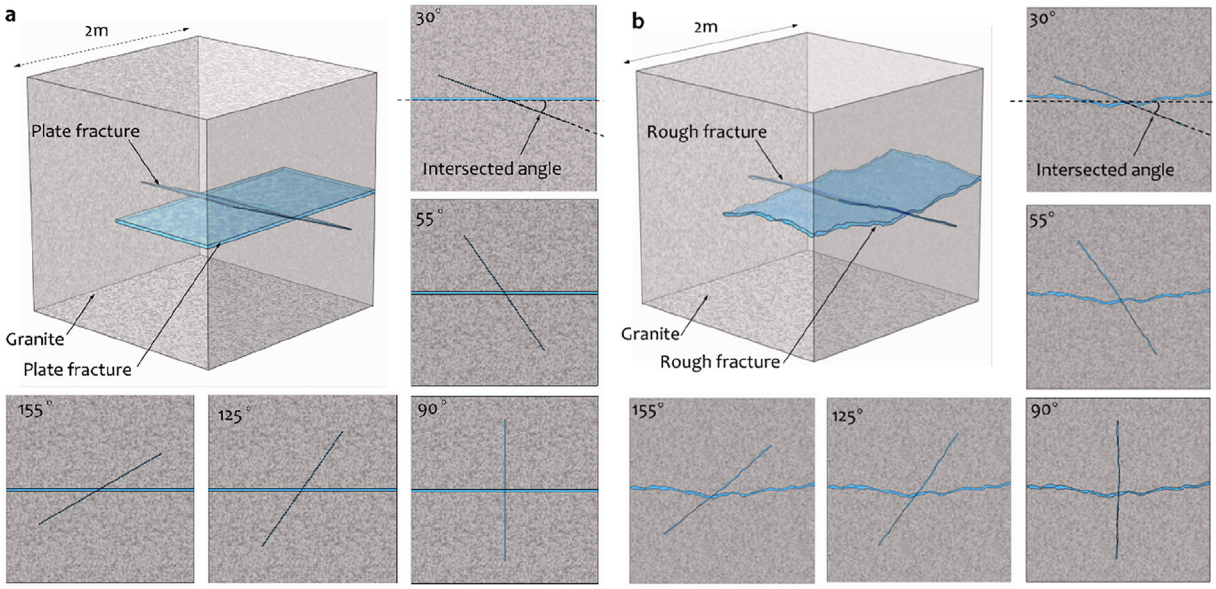

Fig. 7. Intersected (a) plate and (b) rough fracture models with different intersected angles.

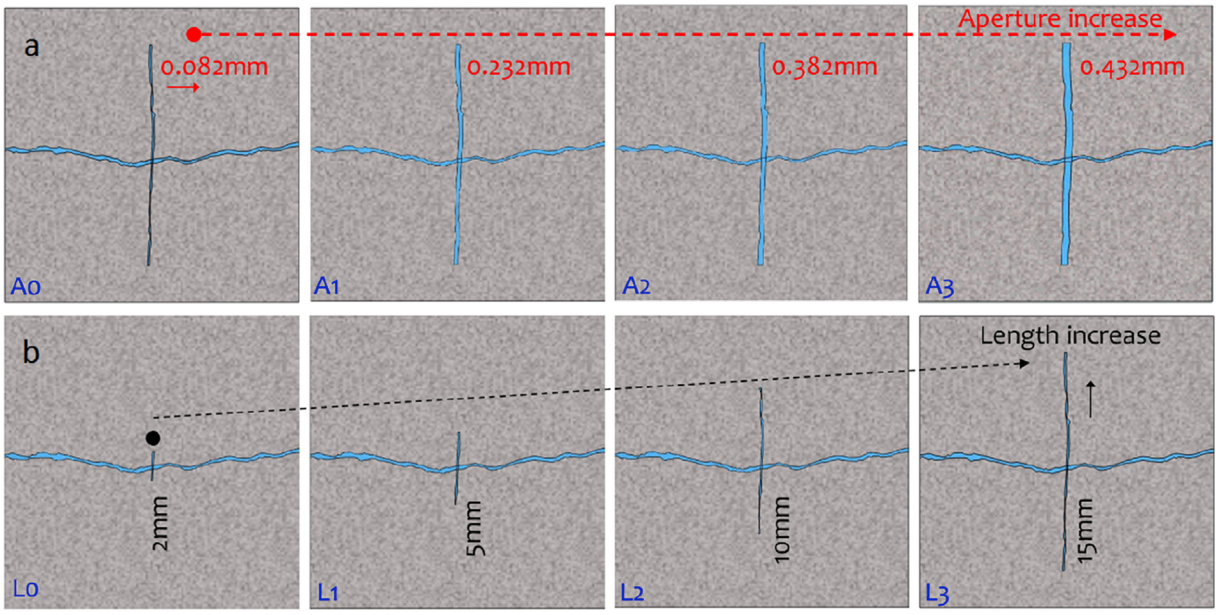

Fig. 8. Intersected rough models with varying (a) apertures and (b) lengths of the DEF.

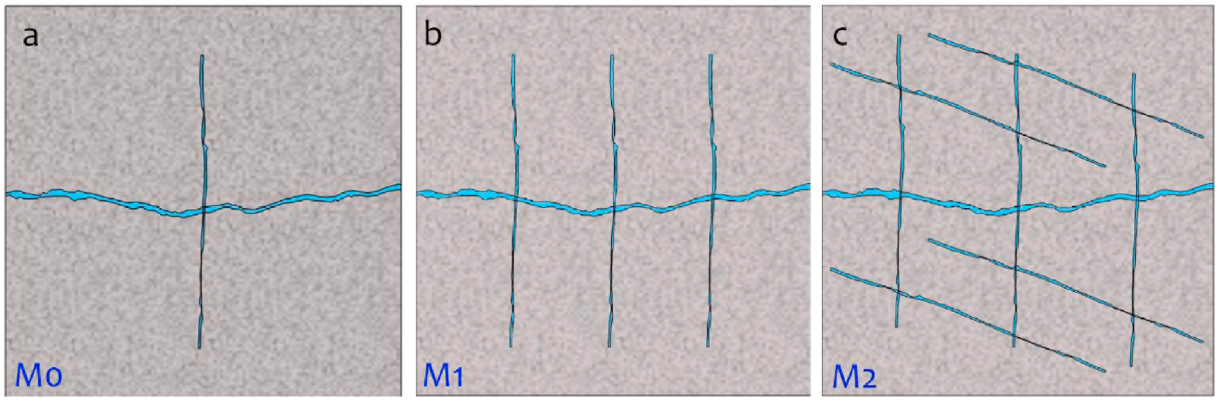

Fig. 9. Computational models of intersected fractures: (a) Single intersected fracture; (b) Three intersected fractures; and (c) Connection of intersected fractures.

3.4. Output parameters

Two characteristic parameters, including the average outlet water temperature T_{out} and the total heat production Q, are defined to characterize the heat transfer performance of the water flowing through intersected fractures.

(1) Average outlet water temperature

The average water outlet temperature T_{out} at the time t is calculated by

$$T_{out}(t) = \frac{\int_{A_{fout}} T_f(x,y,z,t)u(x,y,z)\rho_f\left(x,y,z,T_f\right)C_{p,f}\left(x,y,z,T_f\right)\mathrm{d}A}{\int_{A_{fout}} u(x,y,z)\rho_f\left(x,y,z,T_f\right)C_{p,f}\left(x,y,z,T_f\right)\mathrm{d}A} \tag{6}$$

where A_{fout} is the total area of the outlet; $T_f(x,y,z,t)$ is the water temperature at the location (x,y,z) at time t; and ρ_f and $C_{p,f}$ represent the temperature-dependent density and specific heat capacity of the water, respectively.

Table 2
Geometric information of three modeling scenarios.

Modeling scenario	Intersected angles of DEF to the horizontal MFF (°)	Mechanical aperture of DEF (mm)	Length of DEF (mm)	Number of DEF
I	20	0.082	15	1
	55	0.082	15	1
	90	0.082	15	1
	125	0.082	15	1
	155	0.082	15	1
II	90	0.082	15	1
	90	0.232	15	1
	90	0.382	15	1
	90	0.432	15	1
	90	0.082	2	1
	90	0.082	5	1
	90	0.082	10	1
	90	0.082	15	1
III	90	0.082	15	1
	90	0.082	15	3
	90	0.082	15	7

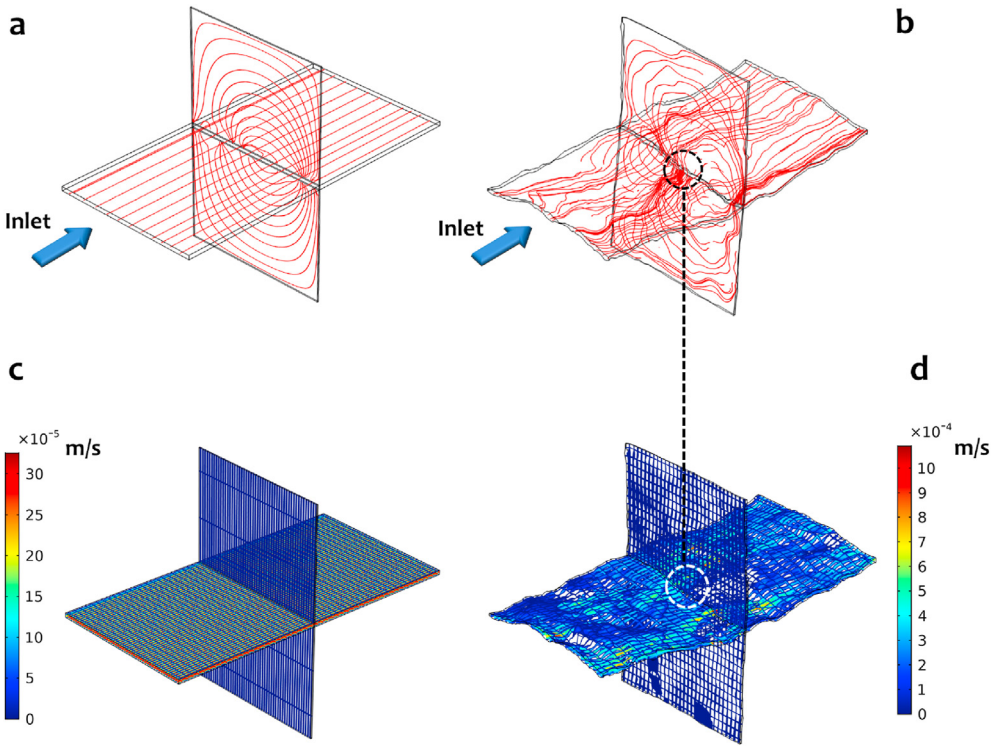

Fig. 10. Distributions of streamlines (a, b) and flow velocities (c, d) in the intersected plate (left) and rough (right) fracture models with the intersected angle of 90° under injection velocity of 0.0002 m/s.

(2) Total heat production

Considering that the heat (Q) absorbed by the water in the whole fracture pathway equals the heat transfer convection between the water and the inner fracture surface, we have

$$Q(t) = H_{\text{out}}M - H_{\text{in}}M \tag{7}$$

where M is the mass flow rate (kg/s); and H_{in} and H_{out} are the fluid enthalpy at the fracture inlet and outlet, respectively:

$$H = T_{\text{f}}(x,y,z,t)C_{\text{p,f}}\left(x,y,z,T_{\text{f}}\right) \tag{8}$$

Furthermore, the cumulative heat production denotes the total heat production during the working periods, which is expressed as

$$Q_{\text{total}} = \int_0^t Q(t)\mathrm{d}t \tag{9}$$

4. Results

4.1. Flow behaviors in 3D intersected fractures

Fig. 10a and b shows the streamlines in the intersected plate and rough models, respectively, under the intersected angle of 90° and injection velocity of 0.0002 m/s. The sectional views of the norm of flow magnitude field, $U = \sqrt{u_x^2 + u_y^2 + u_z^2}$, in the x-, y- and z-directions are plotted in Fig. 10c and d. The streamlines are uniformly distributed along the flow direction in the horizontal MFF of the

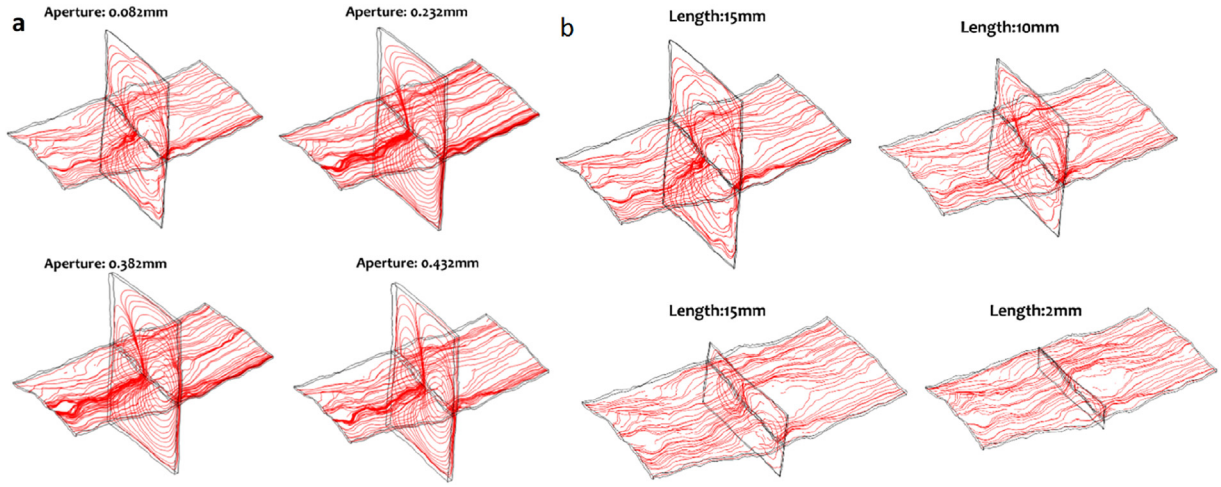

Fig. 11. Distributions of streamlines in intersected rough fracture model with different geometries under injection velocity of 0.0002 m/s.

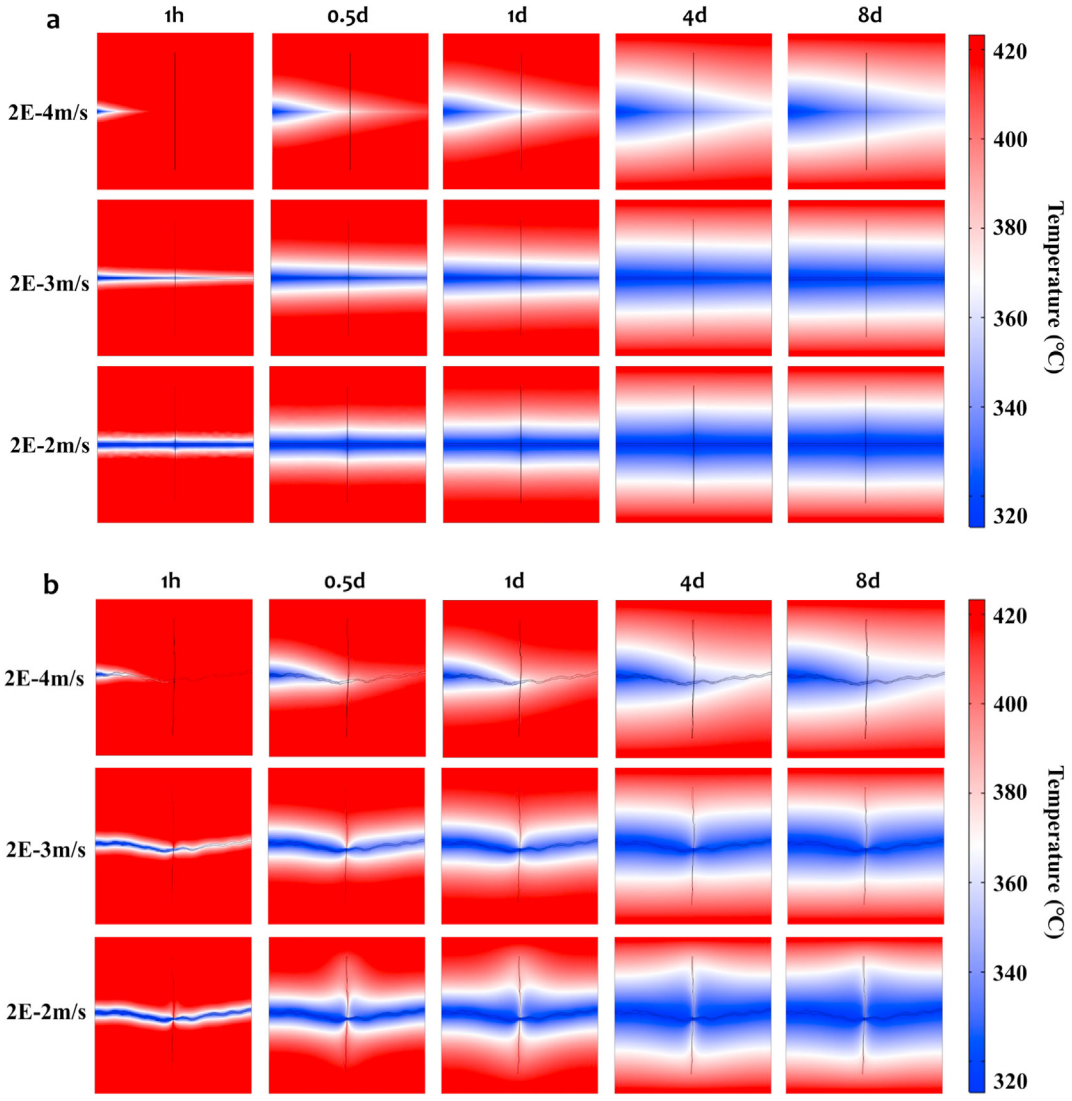

Fig. 12. Temperature distributions changing with the time under the intersected angle of 90° for the (a) plate and (b) rough models.

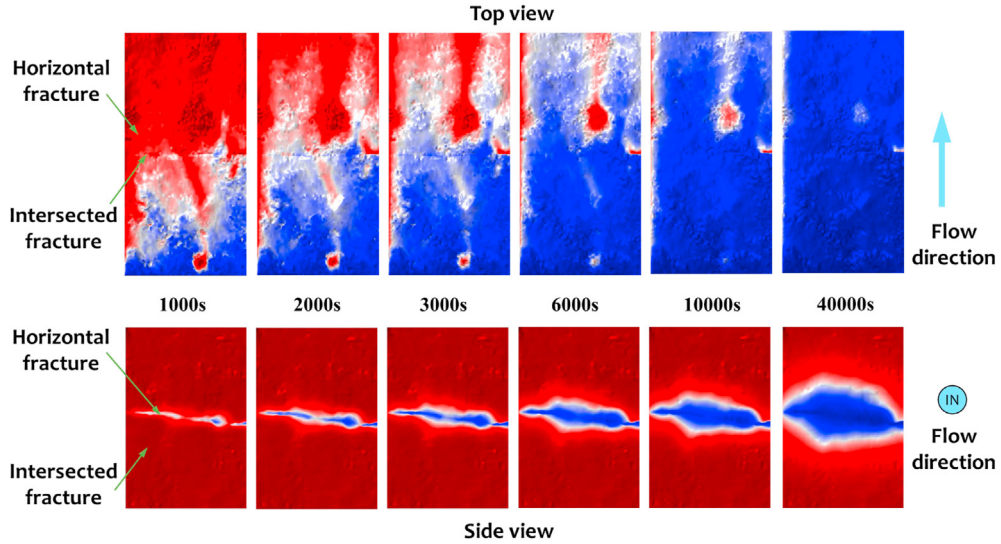

Fig. 13. Temperature distributions along two fractures over the time for case III under the intersected angle of 90° and injection velocity of 0.002 m/s. The scene lighting function in COMSOL was used to clearly show the roughness.

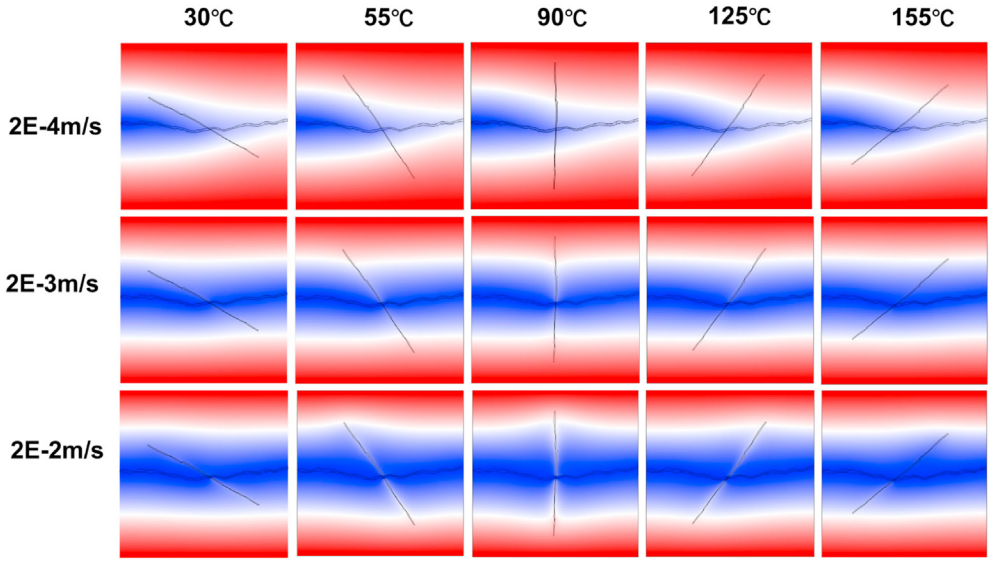

Fig. 14. Temperature distributions in models with various intersected angles under different injection velocities.

plate fracture (Fig. 10a), while present non-uniformly in rough fractures (Fig. 10b), in which a few channels (see the clusters of streamlines) dominate the flow pattern as a result of the heterogeneous distribution of voids in rough fractures. For the rough intersected model, the streamlines flow annularly in and out of the intersected DEF through some discrete local zones at the intersection (black circle in Fig. 10b), resulting in a higher flow velocity at these zones (white circle in Fig. 10d).

Fig. 11 shows the streamlines in intersected rough fractures with different intersected apertures and lengths under the injection velocity of 0.0002 m/s. The channeling effects in the MFF are still the same with the increase of the aperture of the intersected DEF, while the tortuous streamlines become smoother due to the decreasing contact areas at the larger aperture of the intersected DEF. In contrast, the above channeling effects and the tortuosity of streamlines become unobvious with the decrease of the length of intersected DEF, indicating the gradually decreasing influence of the intersected DEF on the fluid flow in rock fractures.

4.2. Temperature distribution in 3D intersected models

Fig. 12 shows the change of rock temperatures with the time in the plate and rough models with the intersected angle of 90° under three injection velocities. A low-temperature zone is formed around the inlet as the water was injected. Upon further increase of the extraction time, the heat stored in the rock is progressively extracted by the flowing water and causes that the low-temperature zone gradually enlarges around the MFF. For the

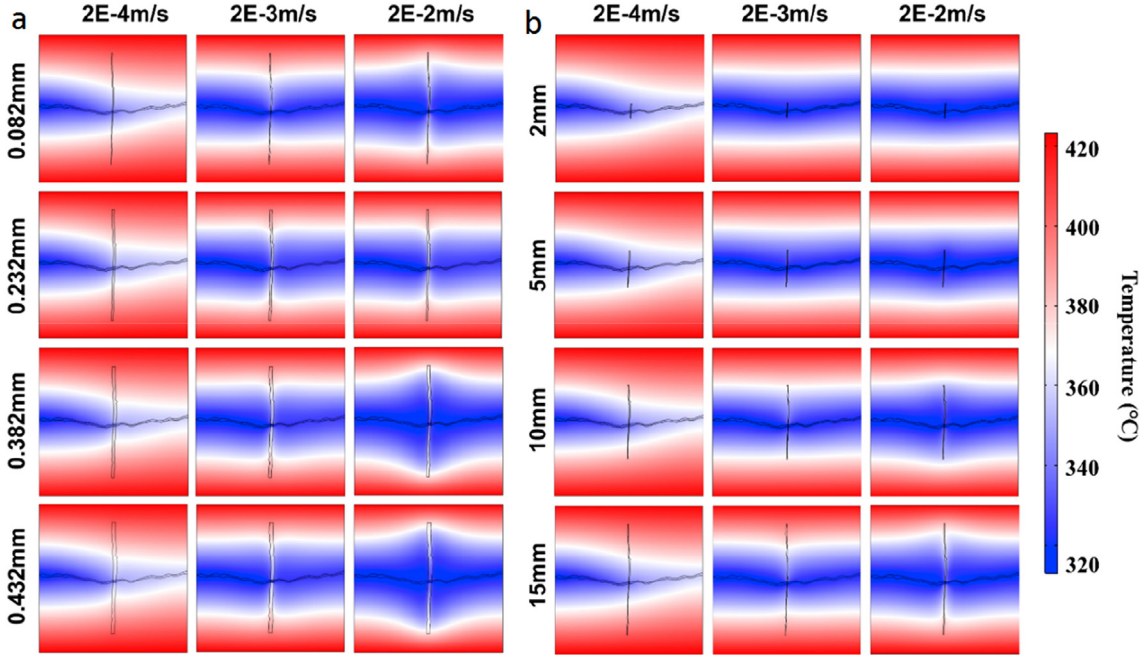

Fig. 15. Temperature distributions in models with various (a) apertures and (b) lengths.

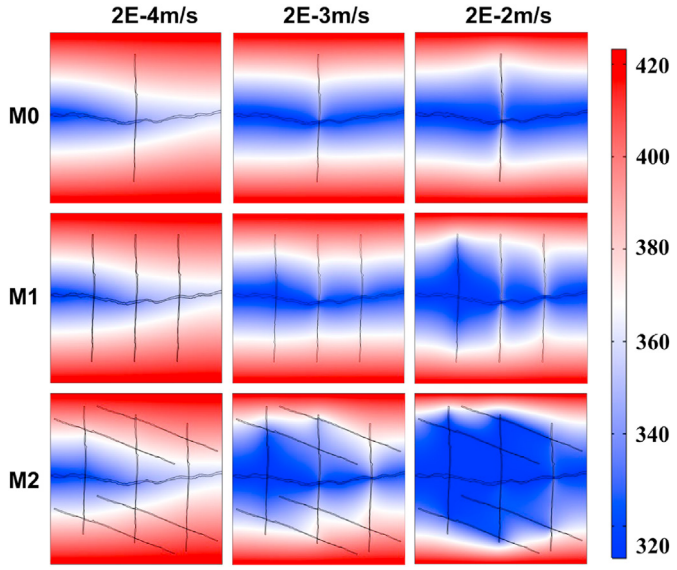

Fig. 16. Temperature distributions after the heat extraction of 10 d for three models under various injection velocities.

intersected plate fracture, the shape of the cold front is the same as that of the heat transfer in the single fracture (He et al., 2019), while in intersected rough fractures, the cold front is different, especially under higher injection velocities. Besides, the distributions of water temperature within the DEF and MFF are shown in the model with the intersected angle of 90° under injection velocity of 0.002 m/s

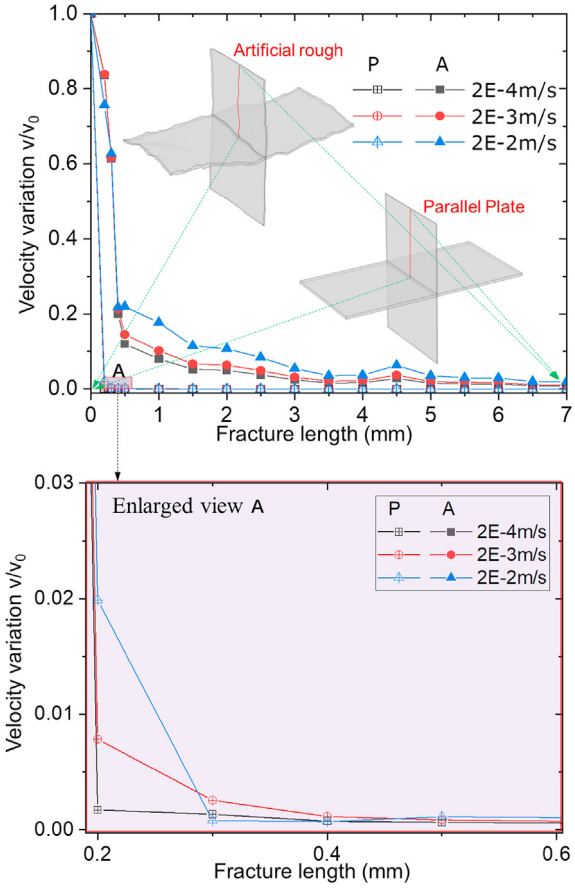

Fig. 17. Flow velocity variations along the half-length of the intersected fracture for plate and rough models under different injection velocities.

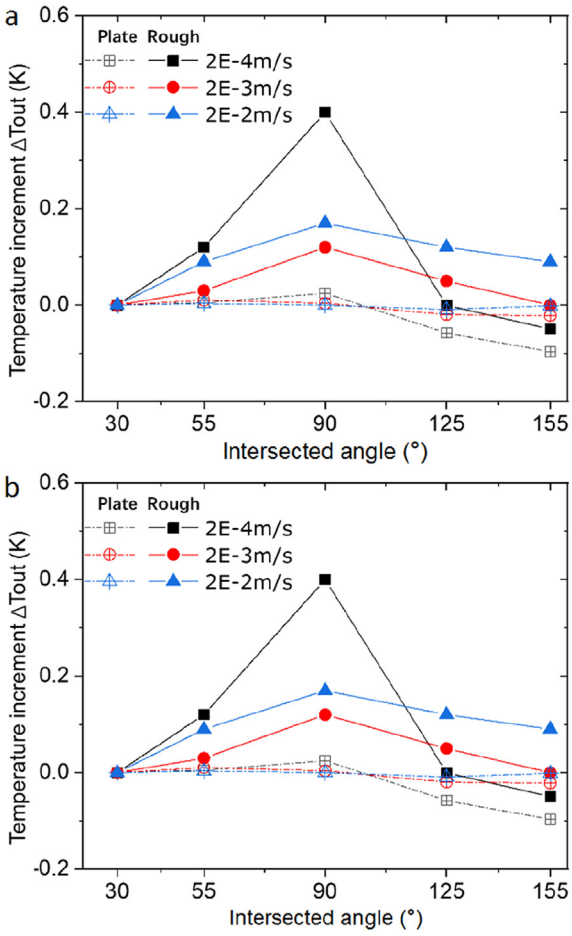

Fig. 18. The outlet temperature increments ΔT_{out} and heat production increment ratio Q/Q_0 versus intersected angles for plate and rough fracture models under different injection velocities.

(Fig. 13). The channeling flow caused by heterogeneous void distributions in the MFF results in a non-uniform evolution of the cold front, and the annular streamlines formed in the intersected DEF lead to an irregular ellipse distribution of the cold front, which gradually extends towards two sides of intersected DEF.

Fig. 14 shows the temperature distributions in models with various intersected angles under the heat extraction of 8 d and different injection velocities. Under the low injection velocity of 0.0002 m/s, the intersected angles have little influence on the evolution of the low-temperature zone. As the injection velocity increases, the low-temperature zone shows the maximum at the intersected angles of 90°. Fig. 15 shows the temperature distributions in intersected rough fractures with different apertures and lengths under the heat extraction of 8 d and different injection velocities. Under each injection velocity, the low-temperature zone is basically the same with the increase of the aperture of intersected DEF, indicating that the increase of aperture of the intersected DEF has little effect on the temperature distribution.

With the increase of the length of the intersected DEF from 2 mm to 15 mm, the low-temperature zones expand significantly towards two walls of the model at the high injection velocity of 0.02 m/s, while they are almost the same at the injection velocities of 0.0002 m/s and 0.002 m/s. This indicates that the increase of the length of the intersected DEF has a significant effect on the temperature distribution under high flow velocity. Fig. 16 shows the temperature distribution in various intersected models M0, M1 and M2, under the heat extraction of 10 d and three injection velocities. The low-temperature

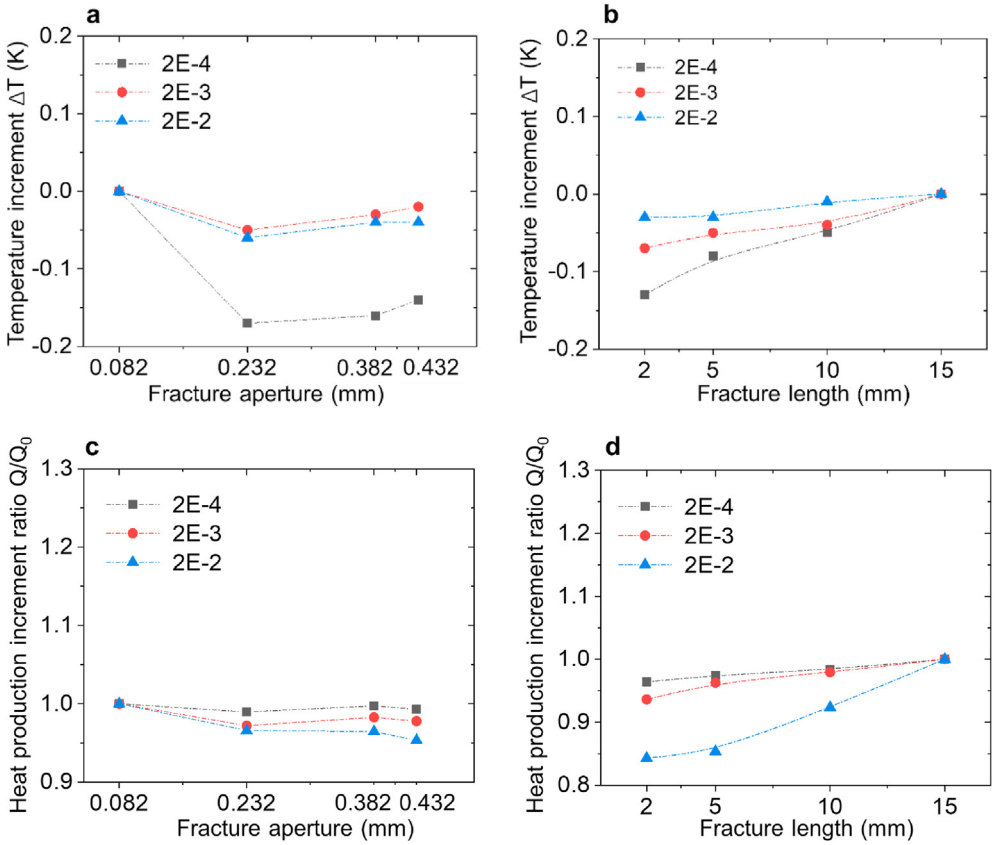

Fig. 19. Changes of the outlet temperature increment ΔT_{out} and heat production increment ratio Q/Q_0 with apertures and lengths of intersected DEF under different injection velocities.

zones are basically the same in three models under the injection velocity of 0.0002 m/s, while as the injection velocity increases to 0.002 m/s and 0.02 m/s, the low-temperature zones expand significantly in models M1 and M2. It shows that the temperature distribution is closely related to both flow velocity and fracture distribution. More discussion regarding these is given below.

5. Discussion

5.1. Flow velocity roles in dead-end fractures

Flow velocity determines the heat transfer through rock fracture (Zhao, 2014). To explore the complicated temperature distribution within intersected rough fractures, the change of velocity variations v/v_0 along the half-length of the intersected DEF in the plate and rough models under different injection flow rates is plotted in Fig. 17, and the enlarged view of the zone A is also given. Here, v/v_0 is defined as the ratio of flow velocity v to the velocity v_0 at the intersection between DEF and MEF. The horizontal axis refers to the length along the intersected DEF. It shows that v/v_0 increases with the injection velocities along the length of DEF in both two models, indicating that the higher the injected rate, the farther the fluid enters the intersected DEF. For the plate fracture, v/v_0 along the intersected DEF decreases rapidly to zero under each injection velocity, while for the rough fracture, v/v_0 decreases rapidly at first and then slowly to zero. v/v_0 along the intersected DEF in the rough model is larger than that in plate one, indicating that the fluid keeps almost still in the intersected plate model but maintains slow flow in the rough one. The change of v/v_0 is correlated with the temperature distribution in intersected DEF as shown in Figs. 11 and 12, indicating that the higher velocities bring a more rapid decrease of the temperature around the intersected DEF and lead to the increase of the low-temperature zone.

5.2. Sensitivity analysis of intersected fracture geometries

5.2.1. Effects of intersected angles

The intersected angle between two rock fractures affects the heat transfer (Ma et al., 2020). The increment of outlet water temperature $\Delta T_{out} = T_{out} - T_0$ and the ratio of heat production $Q_r = Q/Q_0$ changing with the intersected angles for plate and rough models under different injection velocities are plotted in Fig. 18. T_0 and Q_0 refer to the outlet water temperature and heat production, respectively, at the intersected angle of 30° under each injection velocity. Under different intersected angles, ΔT_{out} and Q_r vary significantly in rough fracture models but not obviously in plate ones. For rough models, both ΔT_{out} and Q_r present the largest at the intersected angle of 90°, and they decline with the decrease of the intersected angle between the MFF and DEF. The higher ΔT_{out} and Q_r in rough models indicate that the roughness is beneficial to heat production. The differences of ΔT_{out} and Q_r between two models demonstrate that the geothermal extraction simulation by using plate fractures would misestimate the evolution of temperature and heat production, and the effects of intersected angles on the heat transfer would also be neglected. Regarding the optimization design of fractured reservoirs during developing geothermal resources, the hydraulic fractures need to be created to intersect with natural fractures at large intersected angles for high-efficient geothermal extraction. The underlying mechanism of these

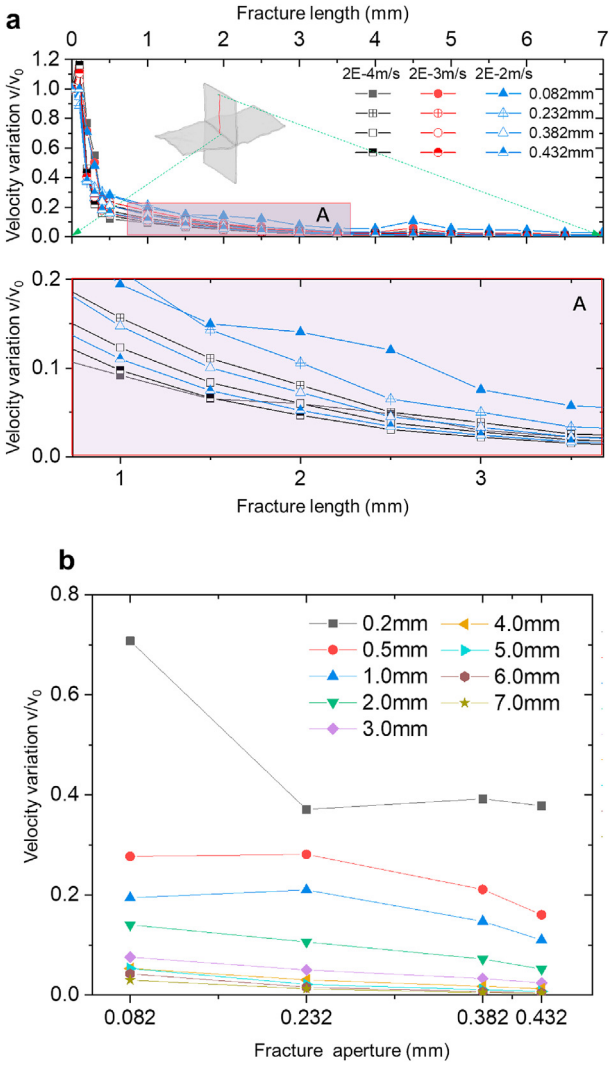

Fig. 20. (a) The change of velocity variation v/v_0 along the half-length of the intersected fracture in models with various apertures, and only 0.0002 m/s (black) and 0.02 m/s (blue) lines are presented in the enlarged figure for clear showing; and (b) The change of velocity variation v/v_0 with fracture aperture at different locations of the intersected DEF, i.e. the distance from the intersection, under the injection velocity of 0.02 m/s.

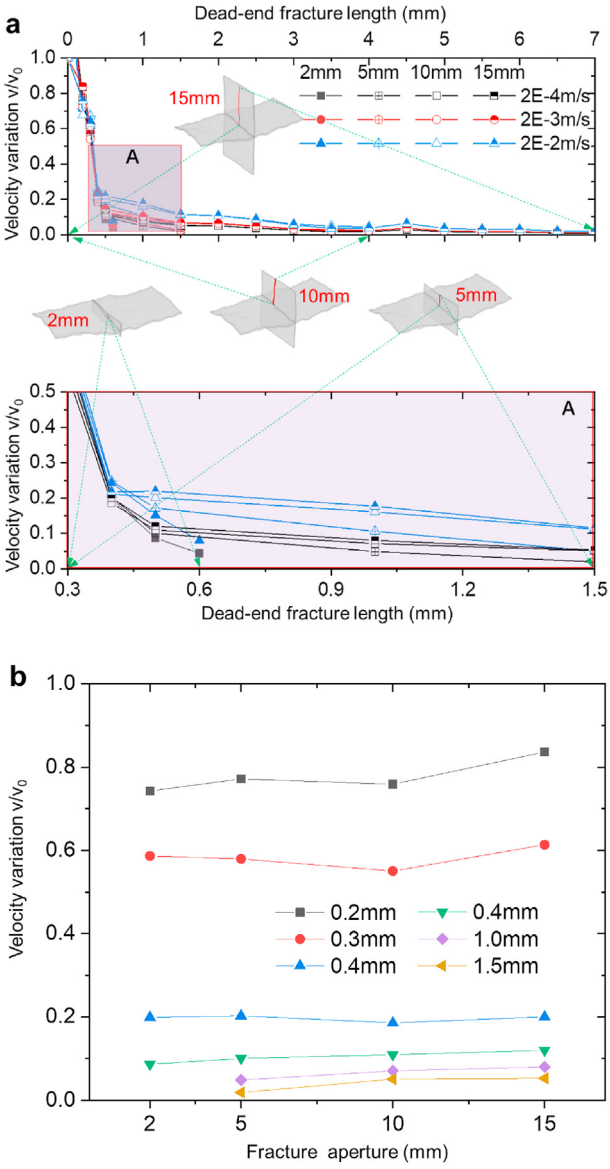

Fig. 21. (a) The change of velocity variation v/v_0 along the half-length of the intersected fracture in models with various lengths, and only 0.0002 m/s (black) and 0.02 m/s (blue) lines are presented in the enlarged figure for clear showing; and (b) The change of velocity variation v/v_0 with fracture length at different locations of the intersected DEF under the injection velocity of 0.0002 m/s.

differences could be ascribed to flow velocity distribution within the intersected fractures.

5.2.2. Effects of apertures and lengths

The aperture and length of the intersected DEF are mainly targeted to be stimulated by using hydraulic fracturing for geothermal exploitation. The increment of outlet water temperature $\Delta T_{out} = T_{out} - T_0$ and the ratio of heat production $Q_r = Q/Q_0$ changing with apertures and lengths of intersected DEF under different injection velocities are plotted in Fig. 19. Here, T_0 and Q_0 refer to the outlet water temperature and heat production of the intersected model with the aperture of 0.082 mm under each injection velocity, respectively. As the fracture aperture increases from 0.082 mm to 0.232 mm, ΔT_{out} and Q_r significantly decrease, and then they vary slightly as the aperture continuously increases to 0.432 mm (Fig. 19a), which would be attributed to the lower velocity formed within the larger aperture of intersected DEF (Fig. 20b). It can be seen that the velocity variation v/v_0 decreases nonlinearly along the half-length of the intersected DEF in models with different apertures (Fig. 20a), and the larger flow velocity in intersected DEF enhances heat transfer and results in larger low-temperature zones in Fig. 15. The flow velocity in intersected DEF decreases with the increase of aperture. With the increase of the length of intersected DEF from 2 mm to 15 mm, ΔT_{out} and Q_r increase (Fig. 19b and d), which can be ascribed to the following two aspects:

(1) The flow velocity in the longer intersected DEF is higher than that at the same location of the shorter DEF, and such difference becomes more apparent under higher injection velocity (as clearly shown in the enlarged view of Fig. 21. The finding conforms to the results in Qu et al. (2017) that the higher flow velocity in intersected DEF enhances the heat transfer from the surrounding rock and raises the spreading scope of the cold front during the circulation of the injection fluid for the heat exploitation.

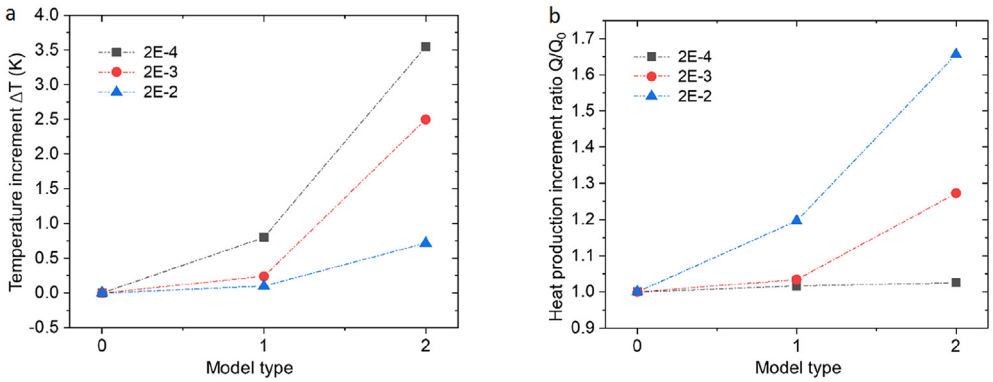

Fig. 22. Changes of the outlet temperature increment ΔT_{out} and heat production increment ratio Q/Q_0 in models M0, M1, and M2 under different injection velocities.

(2) The longer intersected fractures increase the heat transfer area between the fluid flow and the high-temperature rock.

The above result indicates that the extension of the reactivated length of intersected fractures through fracturing techniques is beneficial to the heat production while enhancing the aperture of intersected fractures is not needed. These are helpful to the artificial design of geothermal reservoirs.

5.2.3. Effects of connectivity of intersected fractures

As can be seen in Fig. 16, the connectivity of intersected DEF significantly affects the heat transfer process in fractured reservoirs. Fig. 22 shows the changes of the outlet temperature increment ΔT_{out} and heat production increment ratio Q_r in models M0, M1, and M2 under different injection velocities. Compared to the model M0, the increase of number of intersected DEFs without connectivity between them in the model M1 leads to little increase of ΔT_{out} and Q_r,

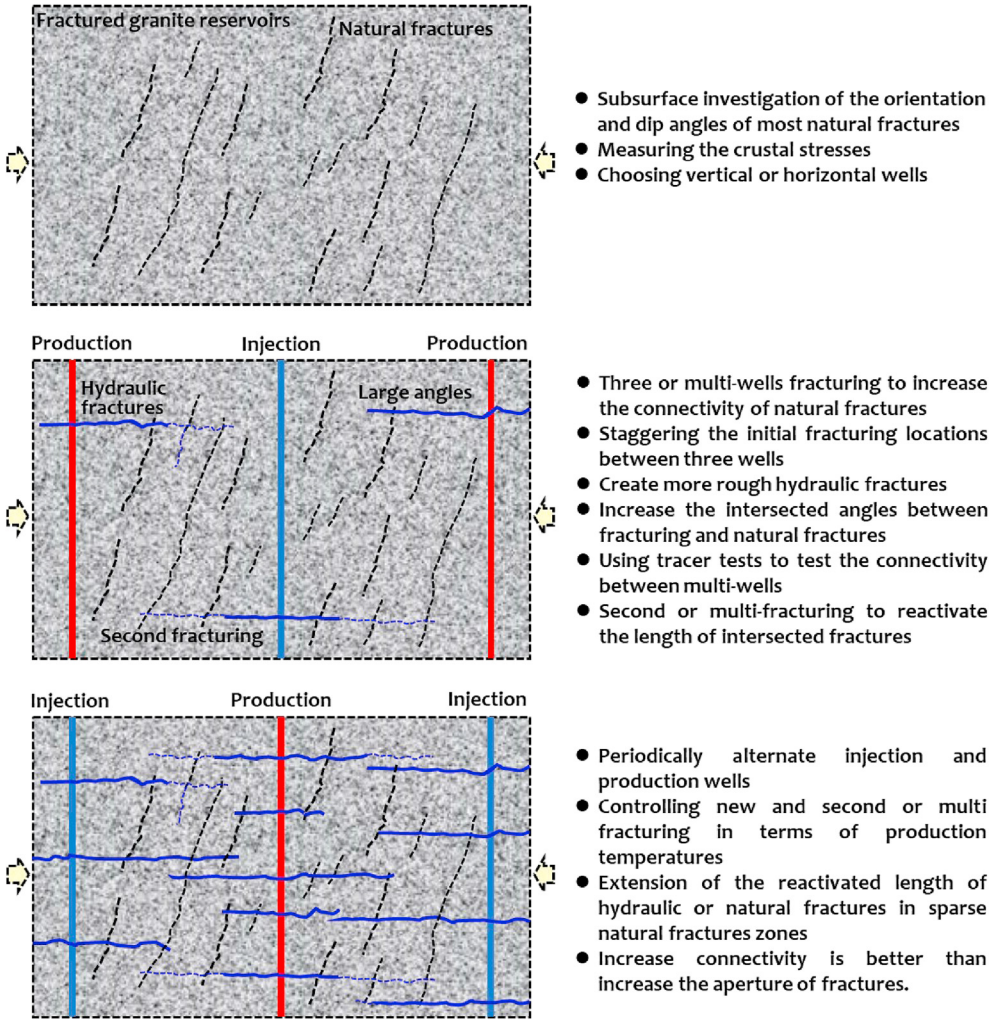

Fig. 23. Schematic hydraulic fracturing design and control for the geothermal extraction.

and more noticeable growth arises in the model M2 under each injection velocity. It indicates that only the increase of number of intersected DEFs by using hydraulic fracturing induces a little increase of heat extraction from geothermal reservoirs if intersected fractures have not been interacted with hydraulic fractures forming the connecting flow path. In contrast, the increase of the connectivity of intersected DEF can significantly prompt heat production. Besides, more connectivity between intersected fractures can also avoid forming preferential flow channels for the working fluid and accelerate the thermal breakthrough.

5.3. Discussion on the intersected fracture design

The DEF at the intersection is usually neglected in the flow or heat transfer simulations regarding subsurface reservoir exploitation (Luo et al., 2016). However, the above simulation indicates that the existing DEFs affect the fluid flow and heat transfer in the MFF. The effective design of intersected fractures is critical to optimal geothermal extraction. Based on simulation results in this study, Fig. 23 gives a schematic design that the hydraulically stimulated fractures connect the pre-existing fractures to form the intersected fractures for enhancing heat extractions. The maximum and minimum principal stresses are along the horizontal and vertical directions, respectively. Three- or multi-well fracturing is needed to increase the connectivity of natural fractures, and the hydraulic fractures should be intersected with natural fractures at large angles. Depending on the change of the production temperature, two- or multi-well fracturing to reactivate the length of intersected fractures is needed, and the injection and production wells should be alternated periodically to avoid forming channeling flows. More simulations regarding the heat transfer in rough fracture networks should be conducted in the future.

6. Limitations

The geothermal exploration modeling requires solving the fully coupled thermo-hydro-mechanical processes in rock fractures (Aliyu and Chen, 2017a), while this study is limited to the coupled hydrothermal modeling of intersected fractured rock mass. Thermoelastic or poroelastic effects should be considered in future research. To balance computational accuracy and efficiency, the model sizes and time scales were 2 m and 10 d, respectively, in this study, and thus upscaling the finding in this study to the real rock fractures in larger sizes and scales in subsurface projects would be an important issue in future studies. In subsurface projects, the connectivity of injection and production wells to the fracture network is also important. This issue has been recently identified in a geothermal field in Iceland where some of the injection wells are underperforming in the vicinity of well-performing wells (Peters et al., 2018; Salimzadeh et al., 2019). Thus, the fracture distributions that affect the change of the connectivity of two wells should also be discussed in the future.

7. Conclusions

In this study, a series of 3D intersected fracture models is constructed to perform the flow-through heat transfer simulation by solving hydrothermal coupling equations. The flow and heat transfer behaviors are investigated to evaluate the influences of intersected geometries of DEF on the heat transfer behavior in terms of heterogeneous apertures, intersected angles, apertures, lengths, and the connectivity. The results provide some insights in determining the main factors affecting the heat transfer characteristics. The following conclusions are drawn:

(1) Intersected DEF significantly affects the flow and heat transfer in the fractured rock mass. Compared to the MFF, the flow velocity in intersected DEF is smaller. The streamlines are uniformly distributed along the flow direction in the horizontal MFF of the plate fracture, while they present non-uniformly in rough fractures. The channeling flow caused by heterogeneous void distributions in the MFF results in a non-uniform evolution of the cold front, and the annular streamlines formed in the intersected DEF lead to an irregular ellipse distribution of the cold front.

(2) The geothermal extraction simulation by using plate fractures would misestimate the evolution of temperature and heat production. The increment of outlet temperature ΔT_{out} and the ratio of hear production Q_r vary significantly in rough fracture models, while this changes are not marked in plate ones. For rough models, both ΔT_{out} and Q_r present the largest at the intersected angle of 90°, and they decline with the decrease of the intersected angle between the MFF and DEF. The higher ΔT_{out} and Q_r in rough models indicate that the roughness is beneficial to heat production. The hydraulic fractures need to be created to intersect with natural fractures at large intersected angles for the optimal design of fracture networks during the geothermal extraction.

(3) The extension of the reactivated length of intersected fractures is beneficial to the heat production while enhancing the aperture of the intersected fracture is not needed. Solely increasing the number of DEF intersected with MFFs induces a little increase of ΔT_{out} and Q_r, and the significant heat extraction can be obtained if the intersected fracture has been interacted with the MFFs forming connecting flow paths.

Declaration of competing interest

The authors declare that they have no known competing financial interests or personal relationships that could have appeared to influence the work reported in this paper.

Acknowledgments

This work was financially supported by the National Key R&D Program of China (Grant No. 2019YFB1504103), and the China Postdoctoral Science Foundation (Grant Nos. 2019TQ0174).

References

Aliyu, M.D., Chen, H.P., 2017a. Optimum control parameters and long-term productivity of geothermal reservoirs using coupled thermo-hydraulic process modelling. Renew. Energy 112, 151–165.
Aliyu, M.D., Chen, H.P., 2017b. Sensitivity analysis of deep geothermal reservoir: effect of reservoir parameters on production temperature. Energy 129, 101–113.
Andrade, J.S., Henrique, E.A.A., Almeida, M.P., Costa, M., 2004. Heat transport through rough channels. Phys. A Stat. Mech. Its Appl. 339, 296–310.
Bakker, R.R., Bruhn, D.F., Barnhoorn, A., 2019. A new laboratory method to measure heat exchange in tensile fractures. In: European Geothermal Congress. Den Haag, The Netherlands, pp. 11–14.
Bear, J., 1972. Dynamics of Fluids in Porous Media. Elsevier, News York, USA.
Cao, W., Huang, W., Jiang, F., 2016. A novel thermal–hydraulic–mechanical model for the enhanced geothermal system heat extraction. Int. J. Heat Mass Tran. 100, 661–671.
Chen, L., Li, J., Zhang, Y., Han, F., Ji, C., Zhang, J., 2019a. Study on coupled heat transfer and seepage in large sparsely fractured surrounding rocks in deep underground spaces. Appl. Therm. Eng. 162, 114277.
Chen, Y., Lian, H., Liang, W., Yang, J., Nguyen, V.P., Bordas, S.P.A., 2019b. The influence of fracture geometry variation on non-Darcy flow in fractures under confining stresses. Int. J. Rock Mech. Min. Sci. 113, 59–71.
Chen, Y., Ma, G., Wang, H., 2018. Heat extraction mechanism in a geothermal reservoir with rough-walled fracture networks. Int. J. Heat Mass Tran. 126, 1083–1093.

Chen, Y., Ma, G., Wang, H., Li, T., Wang, Y., Sun, Z., 2020a. Optimizing heat mining strategies in a fractured geothermal reservoir considering fracture deformation effects. Renew. Energy 148, 326–337.
Chen, Y., Zhang, C., Zhao, Z., Zhao, X., 2020b. Shear behavior of artificial and natural granite fractures after heating and water-cooling treatment. Rock Mech. Rock Eng. 53, 5429–5449.
Chen, Y., Zhao, Z., 2020. Heat transfer in a 3D rough rock fracture with heterogeneous apertures. Int. J. Rock Mech. Min. Sci. 134, 104445.
Freels, J.D., Bodey, I.T., Lowe, K.T., Arimilli, R.V., Lowe, K.T., 2010. Two- Dimensional Thermal Hydraulic Analysis and Benchmark in Support of HFIR LEU Conversion Using COMSOL. Oak Ridge National Laboratory, Oak Ridge, Tennessee, USA. Technical Report ORNL/TM-2010/018.
Fu, P., Hao, Y., Walsh, S.D.C., Carrigan, C.R., 2016. Thermal drawdown-induced flow channeling in fractured geothermal reservoirs. Rock Mech. Rock Eng. 49, 1001–1024.
Gan, Q., Elsworth, D., 2016. Production optimization in fractured geothermal reservoirs by coupled discrete fracture network modeling. Geothermics 62, 131–142.
Gong, F., Guo, T., Sun, W., Li, Z., Yang, B., Chen, Y., Qu, Z., 2020. Evaluation of geothermal energy extraction in Enhanced Geothermal System (EGS) with multiple fracturing horizontal wells (MFHW). Renew. Energy 151, 1339–1351.
Guo, B., Fu, P., Hao, Y., Peters, C.A., Carrigan, C.R., 2016. Thermal drawdown- induced flow channeling in a single fracture in EGS. Geothermics 61, 46–62.
He, R., Rong, G., Tan, J., Cheng, L., 2019. Numerical investigation of fracture morphology effect on heat transfer characteristics of water flow through a single fracture. Geothermics 82, 51–62.
He, Y., Bai, B., Hu, S., Li, X., 2016. Effects of surface roughness on the heat transfer characteristics of water flow through a single granite fracture. Comput. Geotech. 80, 312–321.
Huang, X., Zhu, J., Li, J., Bai, B., Zhang, G., 2016. Fluid friction and heat transfer through a single rough fracture in granitic rock under confining pressure. Int. Commun. Heat Mass Tran. 75, 78–85.
Kadeethum, T., Salimzadeh, S., Nick, H.M., 2019. An investigation of hydromechanical effect on well productivity in fractured porous media using full factorial experimental design. J. Petrol. Sci. Eng. 181, 106233.
Koyama, T., Li, B., Jiang, Y., Jing, L., 2009. Numerical modelling of fluid flow tests in a rock fracture with a special algorithm for contact areas. Comput. Geotech. 36, 291–303.
Lepillier, B., Yoshioka, K., Parisio, F., Bakker, R., Bruhn, D., 2020. Variational Phase–field modeling of hydraulic fracture interaction with natural fractures and application to Enhanced Geothermal Systems. J. Geophys. Res. Solid Earth 125 (7), e2020JB019856.
Liu, G., Pu, H., Zhao, Z., Liu, Y., 2019. Coupled thermo-hydro-mechanical modeling on well pairs in heterogeneous porous geothermal reservoirs. Energy 171, 631–651.
Liu, G., Wang, G., Zhao, Z., Ma, F., 2020. A new well pattern of cluster-layout for deep geothermal reservoirs: case study from the Dezhou geothermal field, China. Renew. Energy 155, 484–499.
Luo, S., Zhao, Z., Peng, H., Pu, H., 2016. The role of fracture surface roughness in macroscopic fluid flow and heat transfer in fractured rocks. Int. J. Rock Mech. Min. Sci. 87, 29–38.
Ma, Y., Zhang, Y., Hu, Z., Yu, Z., Zhou, L., Huang, Y., 2020. Numerical investigation of heat transfer performance of water flowing through a reservoir with two intersecting fractures. Renew. Energy 153, 93–107.
Ma, Y., Zhang, Y., Yu, Z., Huang, Y., Zhang, C., 2018. Heat transfer by water flowing through rough fractures and distribution of local heat transfer coefficient along the flow direction. Int. J. Heat Mass Tran. 119, 139–147.
Nigon, B., 2018. Fracture Flow and Heat Transport Modeling Using Natural Joint Surfaces. PhD Thesis. Ruhr-Universität Bochum (Bochum, Germany).
Peters, E., Blöcher, G., Salimzadeh, S., Egberts, P.J.P., Cacace, M., 2018. Modelling of multi-lateral well geometries for geothermal applications. Adv. Geosci. 45, 209–215.
Pyrak-Nolte, L.J., Nolte, D.D., 2016. Approaching a universal scaling relationship between fracture stiffness and fluid flow. Nat. Commun. 7, 10663.
Qu, Z., Zhang, W., Guo, T., 2017. Influence of different fracture morphology on heat mining performance of enhanced geothermal systems based on COMSOL. Int. J. Hydrogen Energy 42 (29), 18263–18278.
Salimzadeh, S., Grandahl, M., Medetbekova, M., Nick, H.M., 2019. A novel radial jet drilling stimulation technique for enhancing heat recovery from fractured geothermal reservoirs. Renew. Energy 139, 395–409.
Salimzadeh, S., Paluszny, A., Nick, H.M., Zimmerman, R.W., 2018. A three-dimensional coupled thermo-hydro-mechanical model for deformable fractured geothermal systems. Geothermics 71, 212–224.
Sanchez, E.C.M., Cordero, J.A.R., Roehl, D., 2020. Numerical simulation of three-dimensional fracture interaction. Comput. Geotech. 122, 103528.
Selvadurai, A.P.S., Couture, C.B., Rezaei Niya, S.M., 2017. Permeability of wormholes created by CO_2-acidized water flow through stressed carbonate rocks. Phys. Fluids 29, 096604.
Selvadurai, A.P.S., Suvorov, A.P., Selvadurai, P.A., 2015. Thermo-hydro-mechanical processes in fractured rock formations during a glacial advance. Geosci. Model Dev. (GMD) 8, 2167–2185.
Shaik, A.R., Rahman, S.S., Tran, N.H., Tran, T., 2011. Numerical simulation of fluid-rock coupling heat transfer in naturally fractured geothermal system. Appl. Therm. Eng. 31 (10), 1600–1606.
Shi, Y., Song, X., Li, J., Wang, G., Zheng, R., Yulong, F., 2019a. Numerical investigation on heat extraction performance of a multilateral-well enhanced geothermal system with a discrete fracture network. Fuel 244, 207–226.
Shi, Y., Song, X., Wang, G., Li, J., Geng, L., Li, X., 2019b. Numerical study on heat extraction performance of a multilateral-well enhanced geothermal system considering complex hydraulic and natural fractures. Renew. Energy 141, 950–963.
Song, X., Shi, Y., Li, G., Yang, R., Wang, G., Zheng, R., Li, J., Lyu, Z., 2018. Numerical simulation of heat extraction performance in enhanced geothermal system with multilateral wells. Appl. Energy 218, 325–337.
Sun, Z., Zhang, X., Xu, Y., Yao, J., Wang, H., Lv, S., Sun, Z., Huang, Y., Cai, M., Huang, X., 2017. Numerical simulation of the heat extraction in EGS with thermal-hydraulic-mechanical coupling method based on discrete fractures model. Energy 120, 20–33.
Tester, J.W., Anderson, B.J., Batchelor, A.S., Blackwell, D.D., DiPippo, R., Drake, E.M., Garnish, J., Livesay, B., Moore, M.C., Nichols, K., 2006. The Future of Geothermal Energy: Impact of Enhanced Geothermal Systems (EGS) on the United States in the 21st Century. Massachusetts Institute of Technology, Cambridge, Massachusetts, USA.
Turan, A., Saner, S., Artun, E., 2016. Intersecting fracture geometries in control of geothermal spring occurrences in circumferences of the Madra Mountain, Aegean Region of Turkey. In: Geothermal Energy Here and Now: Sustainable, Clean, Flexible, Proceedings of Geothermal Resources Council Annual Meeting (GRC 2016). Curran Associates, Inc., New York, USA, pp. 611–619.
Vidal, J., Genter, A., Chopin, F., 2017. Permeable fracture zones in the hard rocks of the geothermal reservoir at Rittershoffen, France. J. Geophys. Res. Solid Earth 122 (7), 4864–4887.
Vik, H.S., Salimzadeh, S., Nick, H.M., 2018. Heat recovery from multiple-fracture enhanced geothermal systems: the effect of thermoelastic fracture interactions. Renew. Energy 121, 606–622.
Wang, G., Liu, G., Zhao, Z., Liu, Y., Pu, H., 2019. A robust numerical method for modeling multiple wells in city-scale geothermal field based on simplified one-dimensional well model. Renew. Energy 139, 873–894.
Xiong, F., Jiang, Q., Chen, M., 2018. Numerical investigation on hydraulic properties of artificial-splitting granite fractures during normal and shear deformations. Geofluids 2018, 9036028.
Xiong, X., Li, B., Jiang, Y., Koyama, T., Zhang, C., 2011. Experimental and numerical study of the geometrical and hydraulic characteristics of a single rock fracture during shear. Int. J. Rock Mech. Min. Sci. 48 (8), 1292–1302.
Xu, R., Zhang, L., Zhang, F., Jiang, P., 2015. A review on heat transfer and energy conversion in the enhanced geothermal systems with water/CO_2 as working fluid. Int. J. Energy Res. 39 (13), 1722–1741.
Yao, J., Zhang, X., Sun, Z., Huang, Z., Liu, J., Li, Y., Xin, Y., Yan, X., Liu, W., 2018. Numerical simulation of the heat extraction in 3D-EGS with thermal-hydraulic-mechanical coupling method based on discrete fractures model. Geothermics 74, 19–34.
Zhang, J., Xie, J., Liu, X., 2019b. Numerical evaluation of heat extraction for EGS with tree-shaped wells. Int. J. Heat Mass Tran. 134, 296–310.
Zhang, W., Qu, Z., Guo, T., Wang, Z., 2019c. Study of the enhanced geothermal system (EGS) heat mining from variably fractured hot dry rock under thermal stress. Renew. Energy 143, 855–871.
Zhang, Y., Ma, Y., Hu, Z., Lei, H., Bai, L., Lei, Z., Zhang, Q., 2019a. An experimental investigation into the characteristics of hydraulic fracturing and fracture permeability after hydraulic fracturing in granite. Renew. Energy 140, 615–624.
Zhao, Y., Feng, Z., Feng, Z., Yang, D., Liang, W., 2015. THM (thermo-hydro- mechanical) coupled mathematical model of fractured media and numerical simulation of a 3D enhanced geothermal system at 573 K and buried depth 6000–7000 m. Energy 82, 193–205.
Zhao, Z., 2014. On the heat transfer coefficient between rock fracture walls and flowing fluid. Comput. Geotech. 59, 105–111.
Zhou, Z., Jin, Y., Zeng, Y., Zhang, X., Zhou, J., Zhuang, L., Xin, S., 2020. Investigation on fracture creation in hot dry rock geothermal formations of China during hydraulic fracturing. Renew. Energy 153, 301–313.
Zinsalo, J.M., Lamarche, L., Raymond, J., 2020. Injection strategies in an enhanced geothermal system based on discrete fractures model. Appl. Therm. Eng. 169, 114812.
Zou, L., Jing, L., Cvetkovic, V., 2017. Shear-enhanced nonlinear flow in rough-walled rock fractures. Int. J. Rock Mech. Min. Sci. 97, 33–45.